**SUPPORTING INFORMATION**

# Excluded Volume And Weak Interactions In Crowded Solutions Modulate Conformations And RNA Binding Of An Intrinsically Disordered Tail.

Madison A. Stringer[1,2,+], Jasmine Cubuk[1,2,+], J. Jeremías Incicco[1,3], Debjit Roy[1,2], Kathleen B. Hall[1], Melissa D. Stuchell-Brereton[1,2], Andrea Soranno[1,2,*]

[1]*Department of Biochemistry and Molecular Biophysics, Washington University in St Louis, 660 Euclid Ave, 63110, Saint Louis, MO, USA*

[2]*Center for Biomolecular Condensates, Washington University in St Louis, 1 Brookings Drive, 63130, Saint Louis, MO, USA*

[3]current address: *Instituto de Química y Fisicoquímica Biológicas, Universidad de Buenos Aires - CONICET, Junín 956 – 1113, Ciudad de Buenos Aires, Argentina.*

**Corresponding author*

Andrea Soranno: soranno@wustl.edu

[+]:Equal contribution

## REAGENTS.

**Crowding agents.** Ethylene Glycol (EG), PEG 400, PEG 600, PEG 1000, PEG 2050, PEG 4600, PEG 8000 and PEG 35000 were purchased from Sigma Aldrich (USA). PEG 6000 was purchased from Millipore Sigma (USA). PEG 3350 was purchased from INTEGRA Chemical Company (USA).

**Protein and RNA.** RNA used in this study was synthesized and purified with HPLC by IDT technologies (USA). $NTD_L$-RBD and $RBD_L$ were expressed, purified, and labeled as previously described [32,33].

**Cuvette for single-molecule experiments.** Glass cuvettes were assembled using glass cylinders from Hilgenberg (Germany), and coverslips from Deckglaser (Germany), glued together using optical adhesive 61 from Norland (USA), and PEGylated using amino silane from UCT Specialties LLC (USA), sodium bicarbonate from Santa Cruz Biotechnology (USA), and mPEG-SVA from Laysan Bio (USA) as previously described [32].

## INSTRUMENTATION AND DATA ANALYSIS.

**Single-molecule fluorescence setup.** Single-molecule confocal fluorescence measurements were performed using a Picoquant MT200 instrument (Picoquant, Germany). Pulsed Interleaved Excitation (PIE) was obtained by synchronizing a diode laser (LDH-D-C-485, PicoQuant, Germany) and a supercontinuum laser (SuperK Extreme, NKT Photonics, Denmark), filtered by a z582/15 band pass filter (Chroma) and pulsed at 20 MHz. Lasers were focused in the sample through a 60x1.2 UPlanSApo Superapochromat water immersion objective (Olympus, Japan) and emitted photons were collected through the same objective. Separation of

excitation and emission photons was operated by a dichroic mirror (ZT568rpc, Chroma, USA), and emitted photons were further filtered by a long pass filter (HQ500LP, Chroma Technology) to suppress scattering light at wavelength of excitation and by the confocal pinhole (100 µm diameter). Finally, the emitted photons were separated into four channels by a polarizing beam splitter (which differentiate between perpendicular and parallel polarization), followed by a dichroic mirror (585DCXR, Chroma) for each polarization that further select between donor and acceptor photons. Donor and acceptor emission is then filtered using band pass filters, ET525/50m or HQ642/80m (Chroma Technology), respectively, and finally focused on SPAD detectors (Excelitas, USA). The arrival time of every photon is recorded with a HydraHarp 400 TCSPC module (PicoQuant, Germany). FRET experiments are performed by exciting the donor dye with a laser power of 70-100 µW (measured at the back aperture of the objective), whereas acceptor direct excitation is adjusted to match a total emission intensity after acceptor excitation to the one observed upon donor excitation (between 50 and 70 µW). Single-molecule FRET efficiency histograms are acquired at labeled protein concentrations between 50 pM and 300 pM, estimated from dilutions of concentrated samples with known concentration, where concentration was previously determined *via* absorbance measurements.

**Measurement conditions.** All measurements, unless differently specified, were performed in 50 mM HEPES, pH 7.4 at 23°C (NaOH), 200 mM mercaptoethanol, 0.001% v/v Tween20 (for surface passivation) and PEG at the reported concentrations. All measurements were performed in PEGylated glass cuvettes. Each sample was measured for at least 10 min at 23 ± 0.5 °C unless otherwise

indicated. Most measurements were performed at least in duplicate (independent replicates from a new sample preparation) to confirm reproducibility of the results.

**Construction of transfer efficiency histograms.** Fluorescence bursts were identified by time-binning photons in bins of 1 ms and accepting bursts whose total number of photons after donor excitation was larger than at least 15 photons in each bin and contiguous bins were merged if the total number of photons was larger than at least 20 photons.

Transfer efficiencies for each burst were calculated according to

$$E = n_A/(n_A + n_D) \qquad \textbf{Eq. S1}$$

where $n_A$ and $n_D$ are the numbers of donor and acceptor photons, respectively.

Reported transfer efficiencies are corrected for background, acceptor direct excitation, channel crosstalk, differences in detector efficiencies, and quantum yields of the dyes.

Similarly to transfer efficiency, the labeling stoichiometry ratio S is computed accordingly to:

$$S = I_D/(I_D + \gamma_{PIE} I_A) \qquad \textbf{Eq. S2}$$

where $I_D$ and $I_A$ represent the total intensities observed after donor and acceptor excitation and $\gamma_{PIE}$ provides a correction factor to account for the differences between donor and acceptor in detection efficiency and laser intensities. In the

histograms, we present the bursts with stoichiometry corresponding to 1:1 donor:acceptor labeling (in contrast to donor and acceptor only populations), which are selected according to the criterion $0.3 < S < 0.7$. Variations in the selection criteria for the stoichiometry ratio do not impact significantly the observed mean transfer efficiency (within experimental errors).

**Fit of transfer efficiency distributions.** To estimate the mean transfer efficiency and extract multiple populations from the transfer efficiency distributions, each population was approximated with a Gaussian distribution function. When fitting more than one peak, the histogram is analyzed with a sum of two Gaussian functions. In the case of binding of RNA, the two Gaussian distributions associated with the bound and unbound state are constrained to the values of mean transfer efficiency and width of the sample in absence of ligand and at saturation of ligand.

**Estimate of fraction bound.** To estimate the fraction bound and the corresponding $K_A$, we adopted three independent methods. In the first method, we globally fitted the distribution of transfer efficiencies with two Gaussian distributions, one with a fixed conformation determined from the sample in absence of RNA. In the second method, we fitted the mean transfer efficiency of the distribution as it changes with increasing ligand concentration. In the third method, we normalized the histogram and subtract the histogram of the ligand free population from all the subsequent histograms. We then use the area of the population below a threshold given by the “isosbestic” point across the RNA titration to evaluate the fraction bound at each concentration. All three methods provide analogous results on KA as shown in **Fig. S11**.

**Protein dynamics.**

**Nanosecond FCS analysis.** Autocorrelation of acceptor, donor, and cross-correlation curves between acceptor and donor channels were calculated as described previously [56,57]. All measurements were performed at single-molecule concentrations (~300 pM), and donor-only bursts were discarded. Finally, the correlation was computed over a time window of 5 µs, and characteristics timescales were extracted according to:

$$g_{ij}(\tau) = 1 + \frac{1}{M}(1 - c_{AB}Exp[-(\tau - \tau_0)/\tau_{AB}]) \times$$
$$\times (1 + c_{CD}Exp[-(\tau - \tau_0)/\tau_{CD}])(1 + c_{T}Exp[-(\tau - \tau_0)/\tau_{T}]) \quad \textbf{Eq. S3}$$

where *M* is the mean number of molecules in the confocal volume and $i$ and $j$ indicate the type of signal (either from the Acceptor or Donor channels). The three multiplicative terms describe the contribution to amplitude and timescale of photon antibunching (AB), chain dynamics (CD), and triplet blinking of the dyes (T).

**Determination of root mean square interdye distances from mean transfer efficiencies.**

Conversion of mean transfer efficiencies to an interdye distance for fast rearranging ensembles requires the assumption of a distribution of distances. Here we employed the Gaussian model [58]. In the Gaussian model, the conversion rely on one single fitting parameter, the root mean square interdye distance $r = <R^2>^{1/2}$.

Estimates of this parameter is obtained by numerically solving:

$$< E > \; = \int_0^\infty E(R)\, P(R)\, dR \qquad \textbf{Eq. S4}$$

where $R$ is the interdye distance, $P(R)$ represents the chosen distribution, and $E(R)$ is the Förster equation for the dependence of transfer efficiency on distance $R$ and Förster radius $R_0$:

$$E(R) \; = \; \frac{R_0^6}{R_0^6 + R^6} \qquad \textbf{Eq. S5}$$

where $R_0$ denotes the Förster distance for the pair of fluorophores employed (5.4 nm for Alexa Fluor 488/Alexa Fluor 594 in water at 23°C [59]). The Gaussian chain distribution is given by:

$$P(R) \; = \; 4\pi R^2 \left(\frac{3}{2\pi \bar{R}^2}\right)^{3/2} exp\left(-\frac{3R^2}{2\bar{R}^2}\right) \qquad \textbf{Eq. S6}$$

**Eqs. S5** and **S6** are substituted into **Eq. S4** and *r* is numerically optimized such that it equals the experimentally determined value for mean transfer efficiency.

$R_0$ in **Eq. S5** is proportional to the refractive index $r^{-2/3}$ [60] and therefore, upon addition of EG or PEG of different sizes, it is corrected for changes in refractive index according to $R_{0,PEG} = R_0 \, (r_{PEG}/r_0)^{-2/3}$, where $r_0$ is the refractive index in absence of crowders.

Finally, we assessed the effects of crowders on the fluorophore lifetime. As previously reported[14], the effect of PEG on the lifetime of the fluorophores is less than 10% across the concentration range measured. When comparing measurements performed at 15% w/v of crowding agents, the difference between samples has a 5% error, within the range of the error associated to determining the lifetime from burst analysis of multiple measurements. It

should be noted that even if such changes are taken into account, no clear correlation exists between the variations in lifetime and the change observed in conformations. In addition, a correction of 10% in the quantum yield (reflecting the change in lifetime of the donor) would enter in the Förster radius to the power of 1/6, effectively counting only for approximately a 2% to the overall Förster radius [14].

## THEORY.

**Protein conformations.** To capture the competitive effects of the weak interactions of PEG molecules with the protein as well as the excluded volume screening effects due to crowding, we approximated the problem by separating the two contributions. Although weak interactions are favored by the high concentration of polymers, only a small fraction of polymers interact with the protein. These weak interactions are treated analogously to the ones observed for denaturants and osmolytes. By occupying a large fraction of the available volume, the remaining PEG molecules cause screening of the excluded volume of the protein and lead to its compaction.

To describe this type of scheme, we used the approach developed in Hofmann et al. [42], where the conformations of the protein are described by the coil-to-globule model of Sanchez [39], following the work of Sherman and Haran [40] and subsequent modifications [41]. In this framework the degree of compaction of the polymer chain can be described in relation to the theta state configuration as:

$$\alpha^5 - \alpha^3 = \frac{3}{14} N \frac{N b^3}{R_g^3}(1 - \varepsilon) + \frac{N b^3}{R_g^3} \frac{N}{7\alpha^3} \qquad \textbf{Eq. S7}$$

with $\alpha$ being equal to the ratio of the radius of gyration of the protein $R_g$ compared to the radius of gyration of an ideal chain $R_{g\theta}$ and $\varepsilon$ is the interaction energy**,** $N$ is the number of protein monomers, $b$ is the length associated with each monomer.

To be consistent with the definitions used in the renormalization group theory results [25–27] that we will apply later, we define the radius of gyration of the protein in buffer conditions as:

$$R_{g0} = B_N 0.8^{0.5} N^{0.588} \quad \textbf{Eq. S8a}$$

under the assumption that the protein chain is in the good solvent regime. This is the case for our protein chain, which has more expanded configurations than an ideal chain because of repulsive electrostatic interactions. The terms $B_N$ summarizes the specific excluded volume information of the protein chain. We define the ideal reference state as:

$$R_{g\theta} = B_N 0.8^{0.5} N^{0.5} \quad \textbf{Eq. S8b}$$

Based on the definitions in **Eqs. S7** and **S8** we can define an interaction energy for the reference state that is given by:

$$\varepsilon_0 = 1 + b^{-3} B_N^3 \left( \frac{3.34}{N^{0.236}} - \frac{3.34}{N^{0.06}} \right) + 0.93 b^3 B_N^{-3} N^{-0.764} \quad \textbf{Eq. S9}$$

The interaction term can be related to the change in the free energy of solvation through $\Delta\varepsilon = \varepsilon - \varepsilon_0 = \Delta G_{sol}$.

Minimization of **Eq. S7** provides the effect of the contribution of weak protein-PEG interactions to the dimension of the chain, which alters the characteristic excluded volume parameter $B_N$ as

$$B_{N,w} = \alpha\, B_N\, N^{-0.088} \qquad \textbf{Eq. S10}$$

where the subscript $N,w$ is to remember that this quantity is derived in presence of weak interactions.

We can define an analogous quantity for PEG, which is given by

$$B_P = R_g^{PEG}\, 0.8^{-0.5} P^{-0.588} \qquad \textbf{Eq. S11}$$

where $P$ is the number of Kuhn segments in PEG. $R_g^{PEG}$ is given by $R_g^{PEG} = 0.21\left(M_P/M_{P,mon}\right)^{0.583}$ as previously reported in literature [61].

As discussed previously [14,15,18], excluded volume screening can be described using renormalized estimates of the excluded volume parameters for both protein and PEG as well as their relative interaction. To simplify the case scenario, we will use the renormalized theory also for short PEG polymers (according to Flory's criterion): while this is not necessarily accurate, it does not introduce large deviations in the expected trend and restricts the number of variables at play.

With these definitions, we can now define the fundamentals parameters for the renormalized group theory including renormalized values for the number of protein and PEG Kuhn segments ( $N_R$ and $P_R$ , respectively) concentration of PEG ($c_R^P$), and characteristic renormalized length of the protein Kuhn segment ($l_R$):

$$y = \frac{P}{N}\left(\frac{B_P}{B_{N,w}}\right)^{-0.588} \quad \textbf{Eq. S12a}$$

$$s_P = u\, B_P^3 \phi b^{-3} P^{0.76} y^{-0.76} \quad \textbf{Eq. S12b}$$

$$N_R^{-1} + 2\, s_P\, N_R^{-0.76} = 1 \quad \textbf{Eq. S12c}$$

$$P_R = y\, N_R \quad \textbf{Eq. S12d}$$

$$c_R^P = 1/2\,(1 - N_R^{-1}) \quad \textbf{Eq. S12e}$$

$$l_R = B_{N,w}(N/N_R)^{0.588} \quad \textbf{Eq. S12f}$$

$$f_{N,P} = 1 \pm \left(l_R/s_{N,P}\right)^{-0.4} \quad \textbf{Eq. S12g}$$

The interaction between the monomers of PEG and proteins is provided by the $s_{N,P}$ parameter and the associated sign represents compatible vs. incompatible solutions [25,26]. In this case we set $s_{N,P}$ equal to zero to restrict to the case of pure excluded volume interactions. The parameter $u$ is a constant set to be equal to 5.756.

Finally we can compute the root mean square radius of gyration in presence of the excluded volume screening effects of PEG as:

$$R_g^N = \left(l_R^2 N_R\left(0.636 + 0.165\, N_R^{0.5} - 0.292\, N_R^{0.5} f_{N,P} G\left(c_R^P P_R, N_R/P_R\right)\right)\right)^{0.5} \quad \textbf{Eq. S13}$$

where:

$$G(W, y) = W \int_0^\infty z^{-1/2} \frac{B(z)D(zy)}{1 + WD(zy)}\, dz \quad \textbf{Eq. S14a}$$

$$B(z) = \frac{1}{6}e^{-z} - 2D(z) - \frac{8}{z}(D(z) - 1) - \frac{10}{z^2}\left(D(z) - 1 + \frac{z}{3}\right) \quad \textbf{Eq. S14b}$$

$$D(z) = \frac{2}{z^2}\left(e^{-z} - 1 + z\right) \quad \textbf{Eq. S14c}$$

The set of equations **Eqs. S7-S14** is then deployed to fit the experimental dataset across all molecular weights of PEG, from EG to PEG 35000, and all volume fractions. Results are displayed in **Fig. 3B.**

Assuming a relation analogous to the one proposed by Schellman [42,44,45] and assuming the end-groups of PEG and the backbone of PEG interact with independent sites on the protein, we can write :

$$\Delta G_{ee} = \gamma_{ee}\ ln\left[1 + 2\,K_{ee}\left(\phi_{w/v}/M_{P,mon}\right)/\left(M_P/M_{P,mon} + 1\right)\right] \quad \textbf{Eq. S15a}$$

$$\Delta G_{int} = \gamma_{int}\ ln\left[1 + K_{int}\left(\phi_{w/v}/M_{P,mon}\right)\left(M_P/M_{P,mon} - 1\right)/\left(M_P/M_{P,mon} + 1\right)\right] \quad \textbf{Eq. S15b}$$

where here $\gamma_{ee}$ and $\gamma_{int}$ represent the (fractional) number of binding sites associated to each group, $\phi_{w/v}$ is weight per volume concentration, $K_{ee}$ and $K_{int}$ provide the association constant in $mol^{-1}$ units, whereas $M_P$ is the molecular weight of PEG and $M_{P,mon}$ is the molecular weight of the monomer of PEG. Here we approximate $M_{P,mon}$ to 50 Da. For simplicity in the fit we also assume that $K_{ee}$ and $K_{int}$ are similar, $K_{ee} \sim K_{int}$, and the overall difference is encoded in the relative concentration of ends and backbone segments (as rescaled by the length of the polymer) and a change in the number of binding sites. In **Eq. S15**, the volume fraction of the polymer is weighted by fractional occurrence of the ends and backbone elements. For a given polymer

there are $\left(M_P/M_{P,mon} - 1\right)$ backbone elements and 2 ends contribution over a total of $(M_P/M_{P,mon} + 1)$ interacting element per polymer in the solution.

These two different contributions to the free energy are included to account on whether the interaction arises from the PEG end-groups or from the PEG backbone, as previously proposed by the Record lab [49,50], such that

$$\varepsilon = \varepsilon_0 - \Delta G_{ee} - \Delta G_{int} \qquad \textbf{Eq. S16}$$

The linear additivity is a strong simplification of the more complex solvent exchange model for four components in solutions.

**A note regarding the renormalized group theory model.** It is important to note some limitations in the treatment proposed here and corresponding nuances in the renormalized group theory for the ternary solutions. The renormalized theory was developed and is strictly valid for a polymer chain in a solution of longer chains. However, we found that deviations occurring for shorter chains are reasonably small and the convenience of applying a single theory is of greater benefit when including and comparing further elements. Importantly, this theory allows for accounting attractive and repulsive interactions with the crowder. However, we found that the impact of the interaction with shorter PEG molecules (EG and PEG 400), which are attractive and expand the chain, could not be reproduced by the theory, or only in part, using “reasonable” estimates of the interaction parameters. We think this is possibly an intrinsic limitation of the theory that may arise because experimentally there is a difference between generally favorable/unfavorable mixing interactions (implying attractive and repulsive effects) and the physical binding of a ligand to the chain (which increases excluded volume and alters the chain interactions). For this

reason, in this work, we have opted for using the renormalization theory only to establish the pure excluded volume limit and assign to other processes the remaining changes that are observed in the experiments. This obviously is an arbitrary choice, but we think choosing the pure excluded volume limit is a reasonable assumption to provide elements of comparison. This is sustained by the small contribution to chain dimension of other interactions (beyond the effect of pure excluded volume screening) when measuring large PEG polymers. Finally, we want to mention that the theory is solved in the limit of an excluded volume chain and in a mixture of excluded volume chains. While this applies well for PEG, the disordered region is not exactly in the excluded volume limit. In future works, we aim to adapt the theory to capture intermediate regimes between the excluded volume regime and the theta state conditions.

**Flory's criterion.** Application of Flory's criterion for identifying the regime of long *vs* short polymers is partially complicated in this context by the presence of the folded RBD. We assumed an identical segment length for each PEG element and Cα-Cα distance [14]. The interdye distance measured within $NTD_L$-RBD is N=68 residues, which results in $P=N^{1/2}= 8$, equivalent to PEG 400 (assuming a molecular of ~ 50 Da for each monomer of PEG). If we consider the whole $NTD_L$-RBD region, this encompasses N = 173 residues, which results in $P=N^{1/2}= 13$, equivalent to ~ PEG 650. Therefore, we considered PEG 400 and PEG 600 as polymers in the crossover regime, and PEG 1000 (and higher molecular volumes) as "larger" than the protein.

**Protein and nucleic acid binding.** Binding of RNA ligands to labeled N protein constructs in the presence and absence of PEG, was monitored by following the fraction of bursts associated with the bound and unbound population.

When the fraction of bound protein $f_b$ is directly estimated from the distribution of transfer efficiencies, titration curves were analyzed according to:

$$f_b = \frac{K_A[RNA]_{tot}}{1+ K_A[RNA]_{tot}} \quad \textbf{Eq. S17}$$

where $K_A$ is the association constant and $[RNA]_{tot}$ is the total concentration of RNA. Since the protein and $(rU)_{40}$ form a complex with a 1:1 stoichiometry [33] and we measure directly the fractions of free and bound populations not just a signal variation, we can determine $K_A$ with good accuracy from a few points of the titration.

Note that under all conditions the free RNA concentration is always much higher than the concentration of a bound complex because of the single-molecule concentrations of fluorescently labeled protein used in the experiments (~200pM).

**Depletion theory.**

The impact of crowding on the binding of IDRs to ligands has been previously demonstrated by Zosel et al. In brief, the variation in the binding free energies in presence and absence of crowders, $\Delta G$ and $\Delta G_0$ respectively, can be computed by comparing the the equilibrium constants $K_A$ and $K_{A,0}$ according to:

$$\Delta\Delta G = \Delta G - \Delta G_0 = -k_B T ln\frac{K_A}{K_{A,0}} \quad \textbf{Eq. S18}$$

where $k_B$ is the Boltzmann constant and $T$ the temperature in Kelvin.

The osmotic pressure of the solution is given by $\Pi = n\, k_B T$, with $n$ being the number density of colloids. The number density $n$ is linked to the concentration $c$ of colloids

the concentration by $n = c/M$, with $M$ being the molar mass of the crowding agents. The overlap volume $V_{overlap}(r)$ of the colloids depletion layers gives rise to a distance-dependent attractive interaction potential between the colloids, $W(r)$. For two spherical colloidal particles, the binding $\Delta\Delta G$ is equivalent to the interaction potential when the two spheres are brought into contact [62]. This can be computed setting $r$ equal to zero in the interaction potential, i.e. $W(0)$, which leads to:

$$\Delta\Delta G = W(0) = -nk_BTV_{overlap}(0) = -\frac{c}{M}k_BTV_{overlap}(0) \quad \textbf{Eq. S19}$$

where the overlap volume is defined by:

$$V_{overlap}(0) = \frac{\pi(r+R-d)^2(d^2-3(r-R)^2+2d(r+R))}{12d} \quad \textbf{Eq. S20}$$

with [63,64]

$$r = R_1 + \delta_s(R_1) \quad \textbf{Eq. S21a}$$

$$R = R_2 + \delta_s(R_2) \quad \textbf{Eq. S21b}$$

$$d = R_1 + R_2 \quad \textbf{Eq. S21c}$$

$$\frac{\delta_s}{R} = \left(1 + 3\frac{\delta_0}{R} + 2.273\left(\frac{\delta_0}{R}\right)^2 - 0.0975\left(\frac{\delta_0}{R}\right)^3\right)^3 - 1 \quad \textbf{Eq. S21d}$$

$$\delta_0 = 1.07\,R_g \quad \textbf{Eq. S21e}$$

The depletion layer $\delta_0$ accounts for the “soft” nature of the polymer compared to a rigid hard sphere of equivalent radius of gyration $R_g$ .

To account for the crossover of length scales when passing from a dilute to a semidilute solution, an effective depletion layer $\delta$ is defined as:

$$\delta^{-2} = \delta_0^{-2} + \xi^{-2} \qquad \textbf{Eq. S22}$$

where $\delta_0$ is the depletion layer in a dilute solutions and $\xi$ is the average mesh size of the polymer solution in the semidilute regime [65].

**SUPPLEMENTARY FIGURES.**

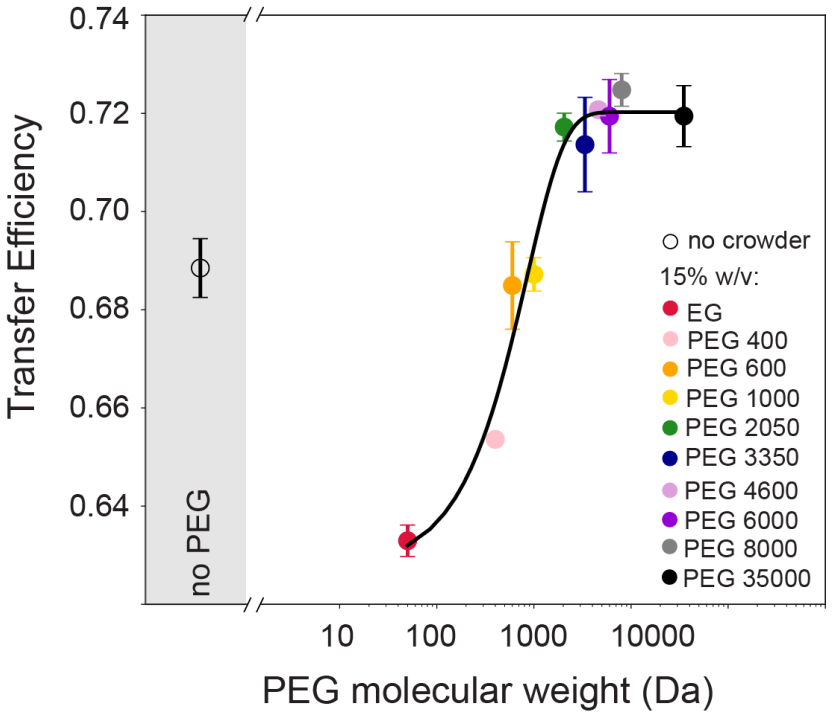


**Figure S1. Mean transfer efficiency at 15% w/v as a function of PEG Molecular Weight.** Line is a guide for the eyes.

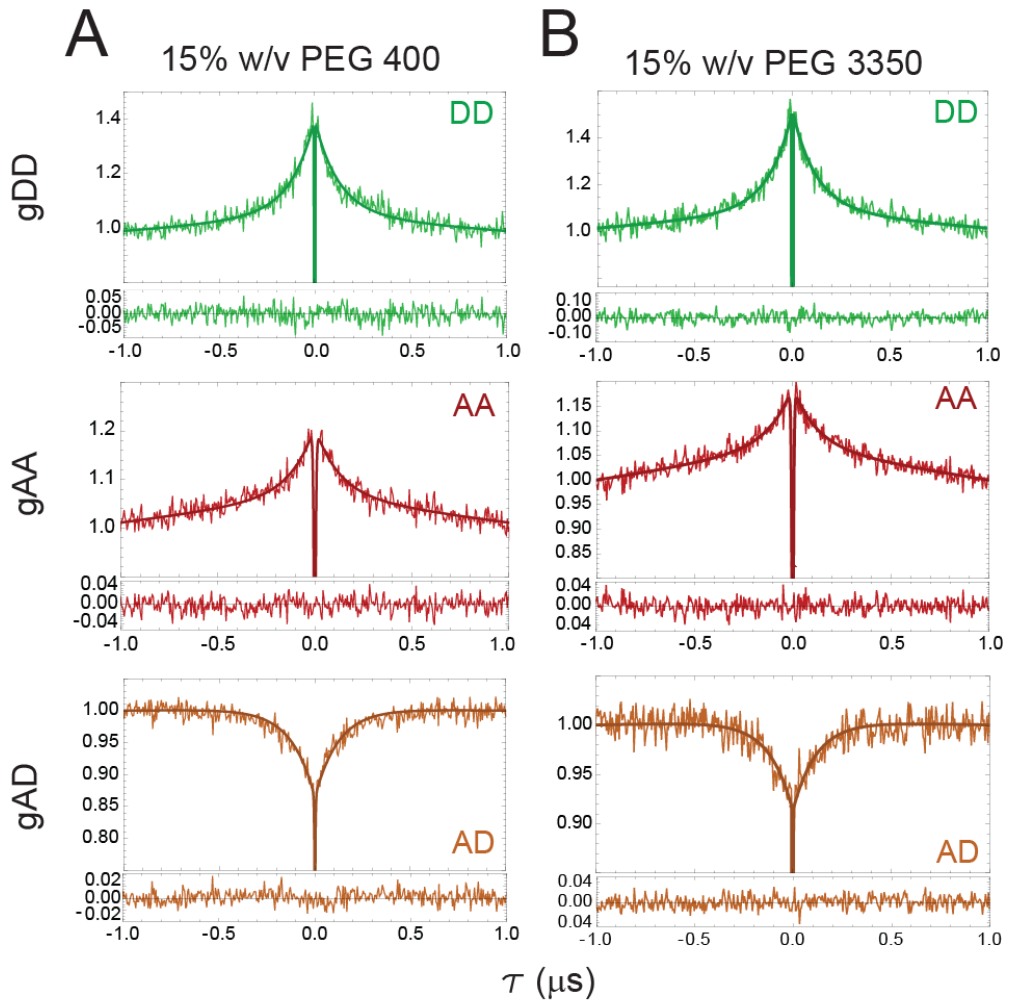


**Figure S2. $NTD_L$-RBD dynamics under crowding conditions.** Example of nanosecond-FCS (nsFCS) traces of $NTD_L$-RBD in the presence of 15% w/v PEG 400 (**A**) and PEG 3350 (**B**) solutions. Donor-donor, acceptor-acceptor, and donor-acceptor correlations are shown in green, red, and orange (respectively). Solid lines report about a global fit to **Eq. S3** and corresponding residuals.

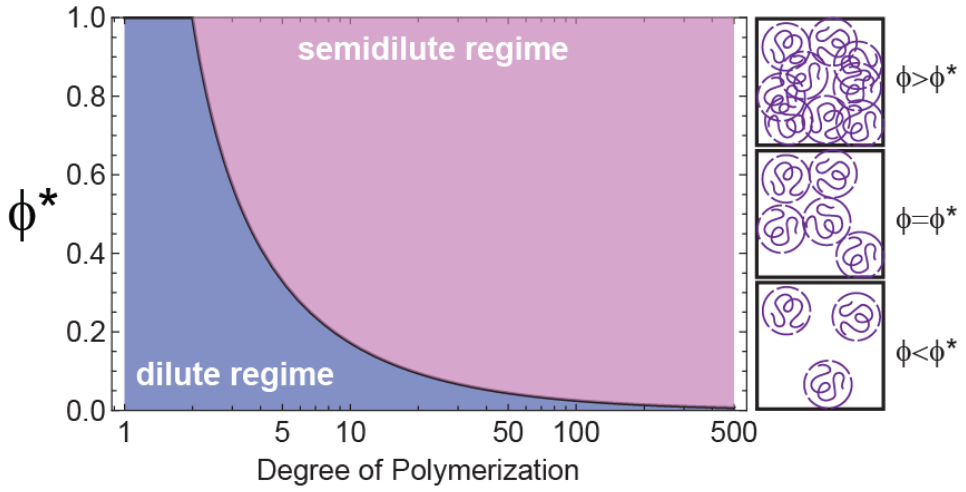


**Figure S3. Dilute and semidilute regimes.** Schematic of the overlap concentration $\phi^*$ as a function of the degree of polymerization (number of monomers) of the PEG molecule.

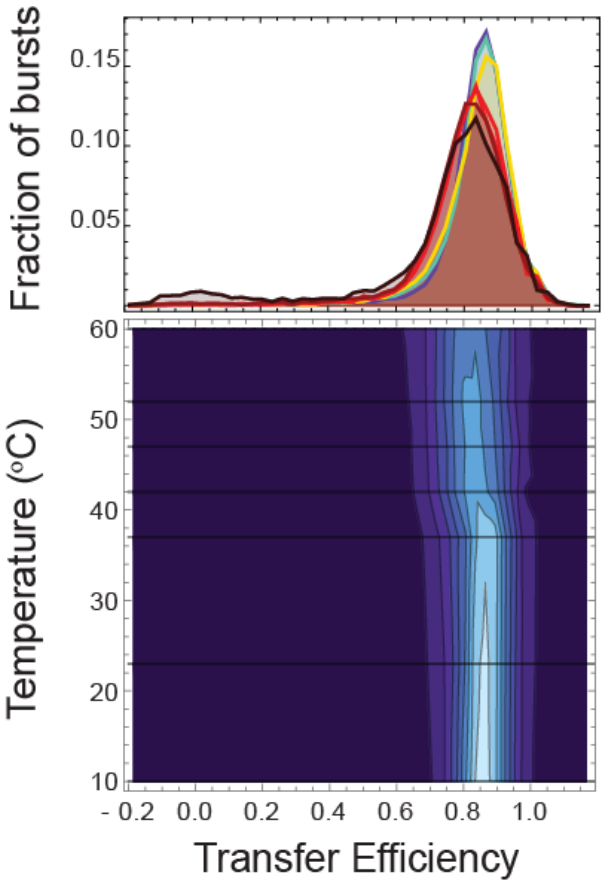


**Figure S4. Temperature dependence of $RBD_L$.** *Upper panel.* Representative transfer efficiency distributions of $RBD_L$ in 50 mM HEPES buffer. *Lower panel.* Corresponding contour plot as a function of temperature and transfer efficiency. Solid lines represent measured temperatures. A transition occurs between 37 and 43 °C with a clear shift of transfer efficiencies to lower values. The trend is opposite to what is observed for $NTD_L$-RBD and suggests a conformational change in the RBD. The specific shift in transfer efficiency is reminiscent of the intermediate state populated at low denaturant concentrations [32,33].

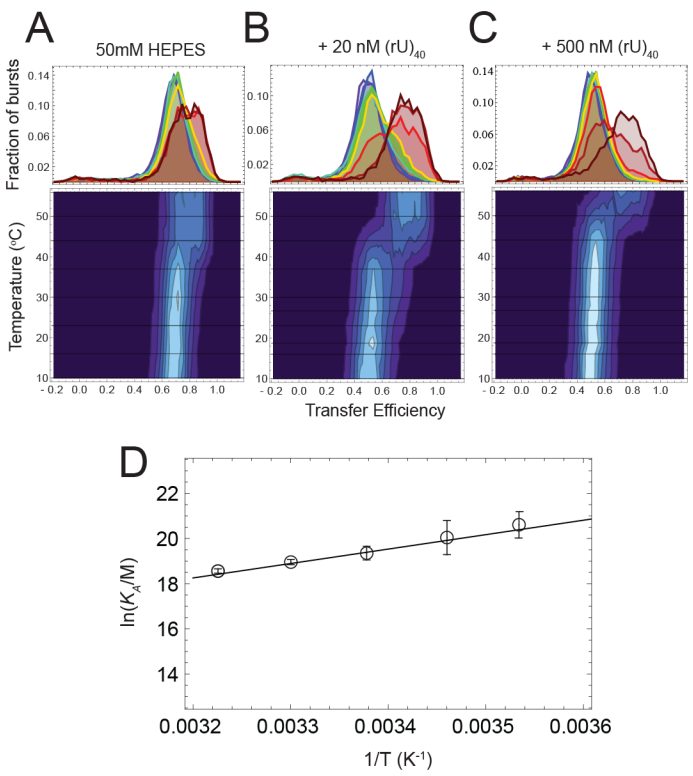


**Figure S5. NTD-RBD conformations and binding of $(rU)_{40}$ as a function of temperature. A-C.** *Upper panels.* Representative transfer efficiency distributions of the $NTD_L$-RBD in 50 mM HEPES buffer (**A**), with addition of 20 nM $(rU)_{40}$ (**B**), and with addition of 500 nM $(rU)_{40}$ (**C**) as a function of temperature from 10 °C to 56 °C. *Lower panels.* Contour plots of the transfer efficiency distributions of $NTD_L$-RBD as a function of temperature for the corresponding experimental conditions in the upper panels. **D.** Plot of the $\log(K_A/nM)$ as a function of 1/T ($K^{-1}$). Error bars represent error of the fit when calculating $K_A$ as a function in changes in transfer efficiency. The linear fit reports about the enthalpy (slope) and entropy (intercept) of binding according to **Eq. 4**. Fitting results are reported in **Table S7 and S8**.

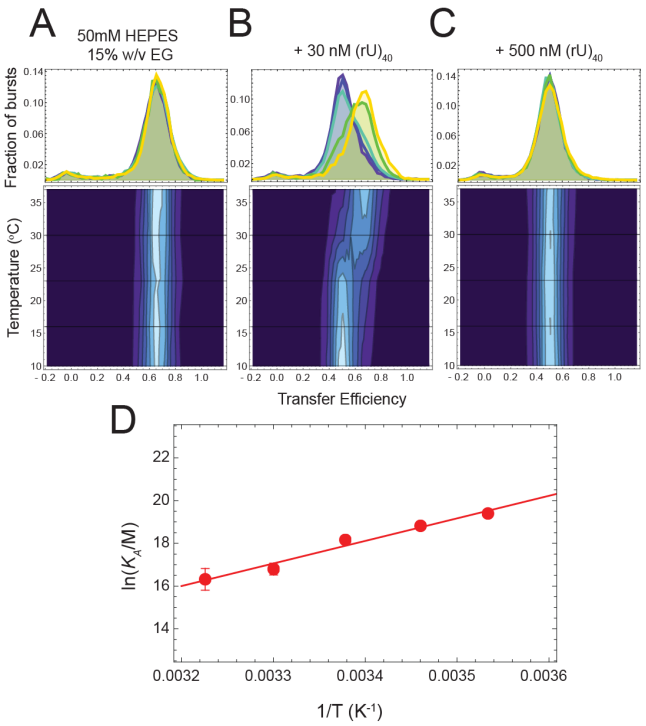


**Figure S6. NTD-RBD conformations and binding of $(rU)_{40}$ as a function of temperature in the presence of 15% w/v EG. A-C.** *Upper panels.* Representative transfer efficiency distributions of the $NTD_L$-RBD in 50 mM HEPES, 15% w/v EG buffer (**A**), with addition of 30 nM $(rU)_{40}$ (**B**), and with addition of 500 nM $(rU)_{40}$ (**C**) as a function of temperature from 10 °C to 37°C. *Lower panels.* Contour plots of the transfer efficiency distributions of $NTD_L$-RBD as a function of temperature for the corresponding experimental conditions in the upper panels. **D.** Plot of the $\log(K_A/nM)$ as a function of 1/T ($K^{-1}$). Error bars represent errors of the fit. The linear fit reports about the enthalpy (slope) and entropy (intercept) of binding according to **Eq. 4**. Fitting results are reported in **Table S7 and S8**.

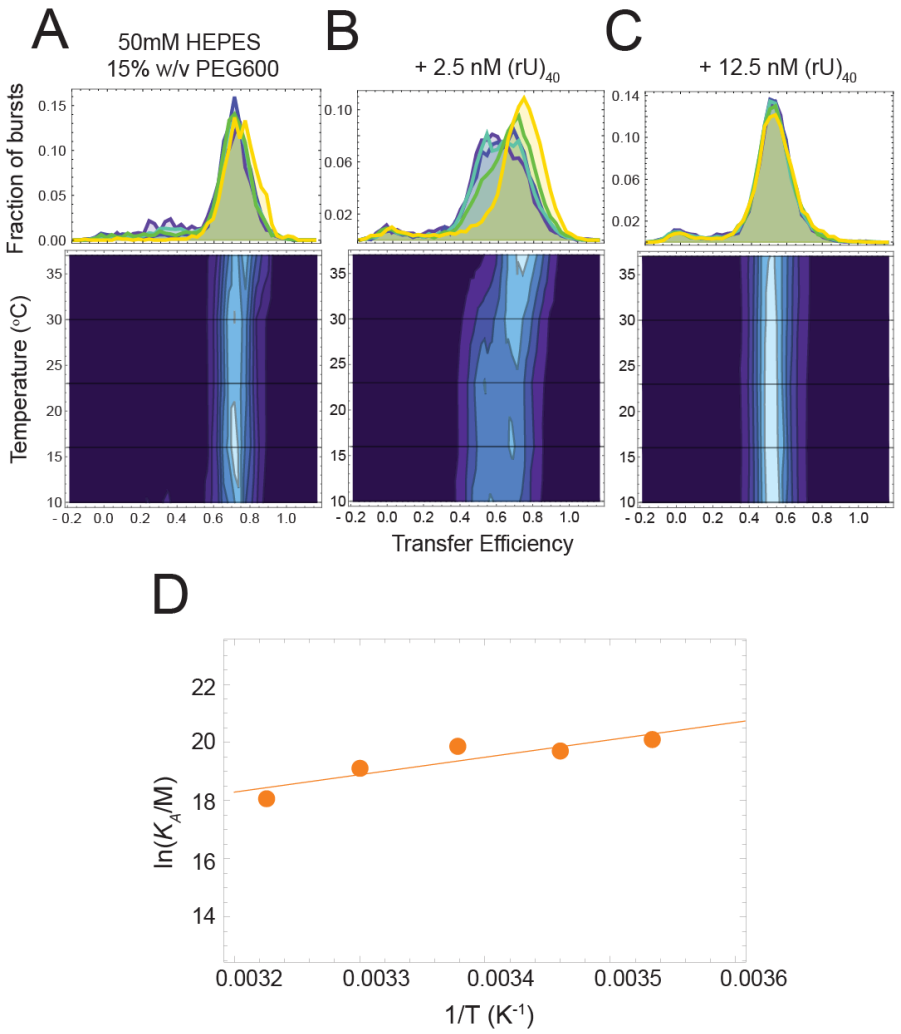


**Figure S7. NTD-RBD conformations and binding of $(rU)_{40}$ as a function of temperature in the presence of 15% w/v PEG 600. A-C.** *Upper panels.* Representative transfer efficiency distributions of the $NTD_L$-RBD in 50 mM HEPES buffer (**A**), with addition of 2.5 nM $(rU)_{40}$ (**B**), and with addition of 12.5 nM $(rU)_{40}$ (**C**) as a function of temperature from 10 °C to 37 °C. *Lower panels.* Contour plots of the transfer efficiency distributions of $NTD_L$-RBD as a function of temperature for the corresponding experimental conditions in the upper panels. **D.** Plot of the $\log(K_A/nM)$ as a function of 1/T ($K^{-1}$). Error bars represent errors of the fit. The linear fit reports about the enthalpy (slope) and entropy (intercept) of binding according to **Eq. 4**. Fitting results are reported in **Table S7 and S8**.

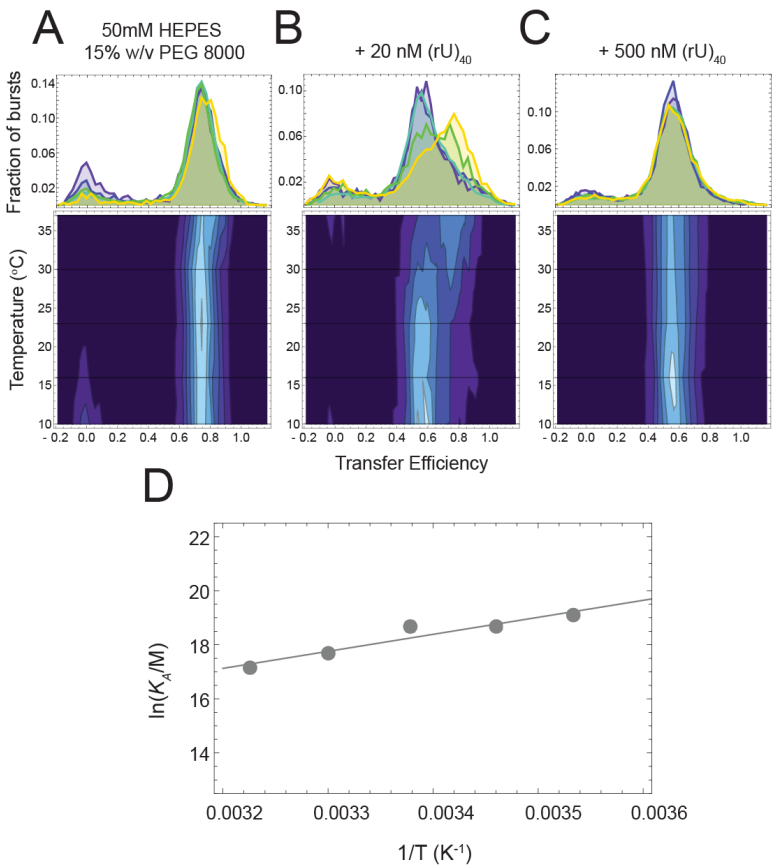


**Figure S8. NTD-RBD conformations and binding of $(rU)_{40}$ as a function of temperature in the presence of 15% w/v PEG 8000. A-C.** *Upper panels.* Representative transfer efficiency distributions of the $NTD_L$-RBD in 50 mM HEPES buffer (**A**), with addition of 20 nM $(rU)_{40}$ (**B**), and with addition of 500 nM $(rU)_{40}$ (**C**) as a function of temperature from 10 °C to 37 °C. *Lower panels.* Contour plots of the transfer efficiency distributions of $NTD_L$-RBD as a function of temperature for the corresponding experimental conditions in the upper panels. **D.** Plot of the $\log(K_A/nM)$ as a function of 1/T ($K^{-1}$). Error bars represent errors of the fit. The linear fit reports about the enthalpy (slope) and entropy (intercept) of binding according to **Eq. 4**. Fitting results are reported in **Tables S7 and S8**.

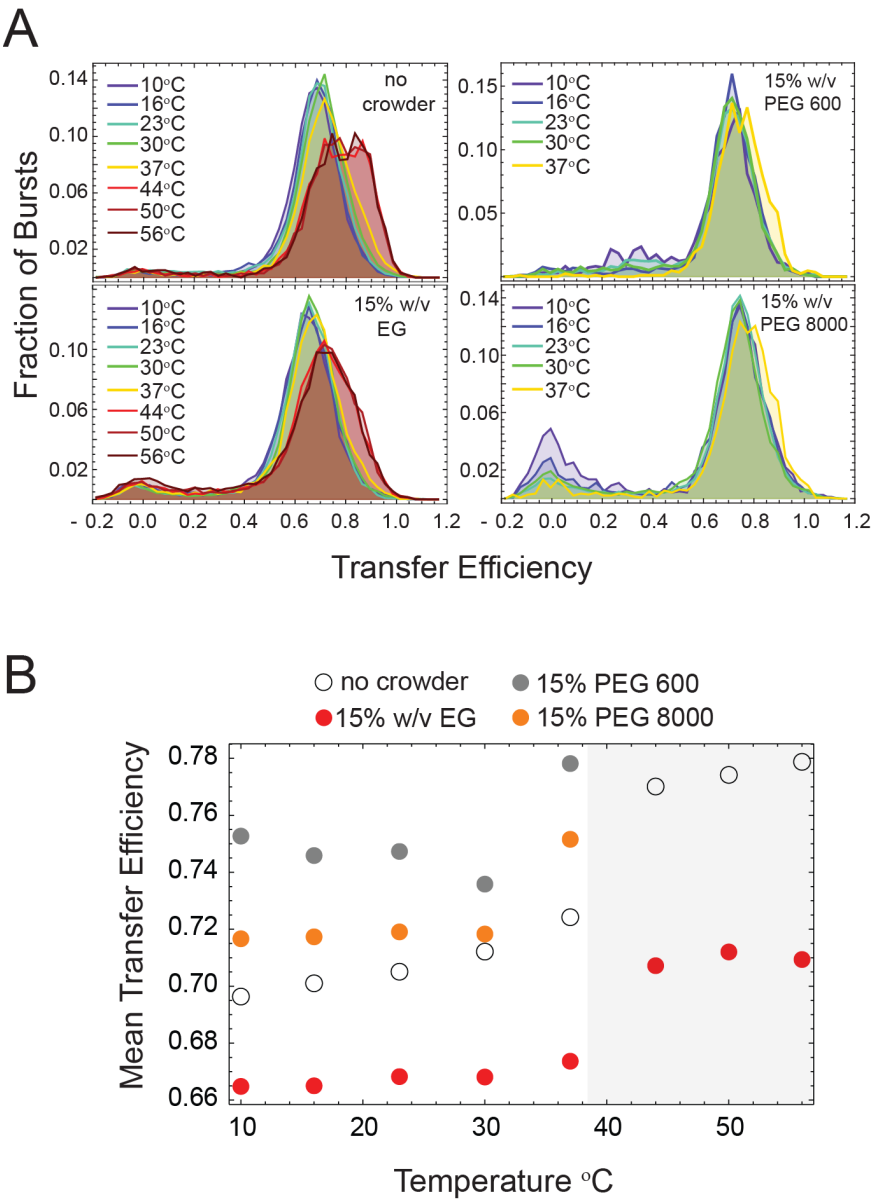


**Figure S9. $NTD_L$-RBD conformations as a function of temperature in absence and presence of 15% w/v PEG solutions.** **A.** Representative histograms of conformational changes in absence of crowders, 15% w/v EG, PEG 600, and PEG 8000. **B.** Corresponding mean transfer efficiencies as function of the temperature. The gray area represents the region where a second conformation is absence of crowding. Addition of large crowders shifts the transition toward lower temperatures as indicated by the sudden increase in transfer efficiency at 37 C.

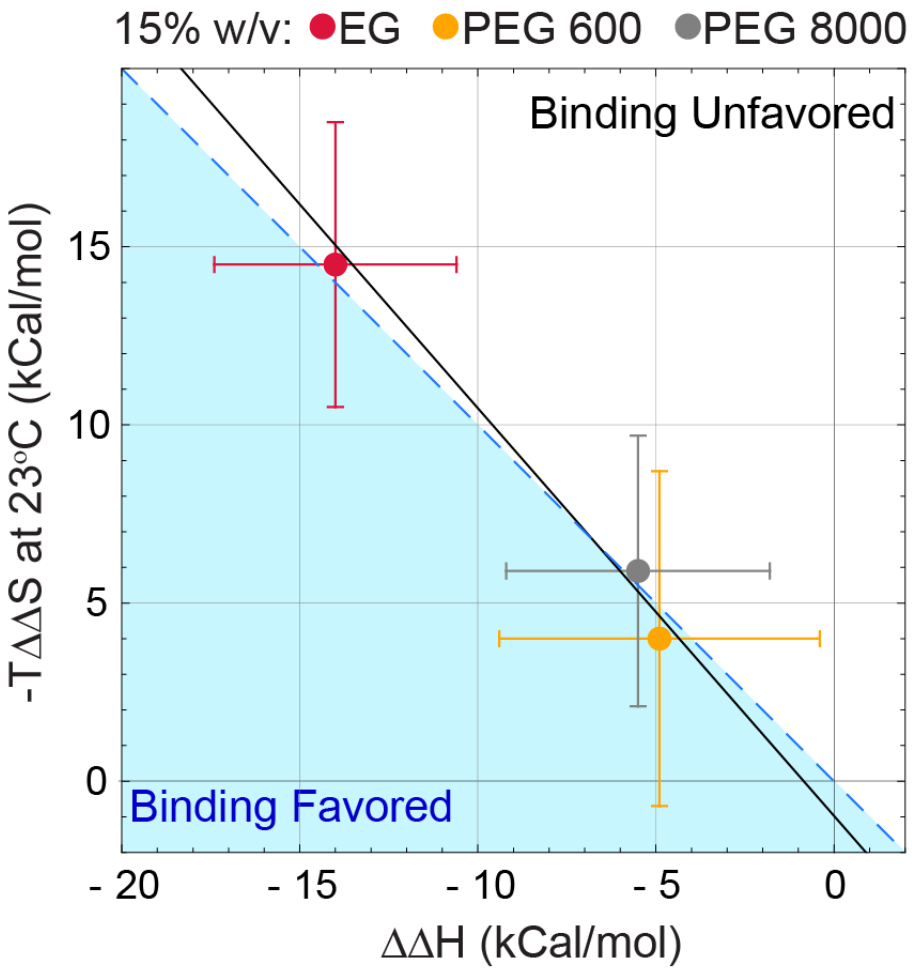


**Figure S10. ΔΔH and -TΔΔS at 15% w/v for EG** (red)**, PEG 600** (yellow)**, PEG 8000** (gray)**.** Cyan area indicates the region where binding is favored, the white one, the area where binding is unfavored. The measured values for EG, PEG 600, and PEG 8000 lie on a line (black line) parallel to the bisectrix (red line). Error bars are propagated from the errors on ΔH and ΔS.

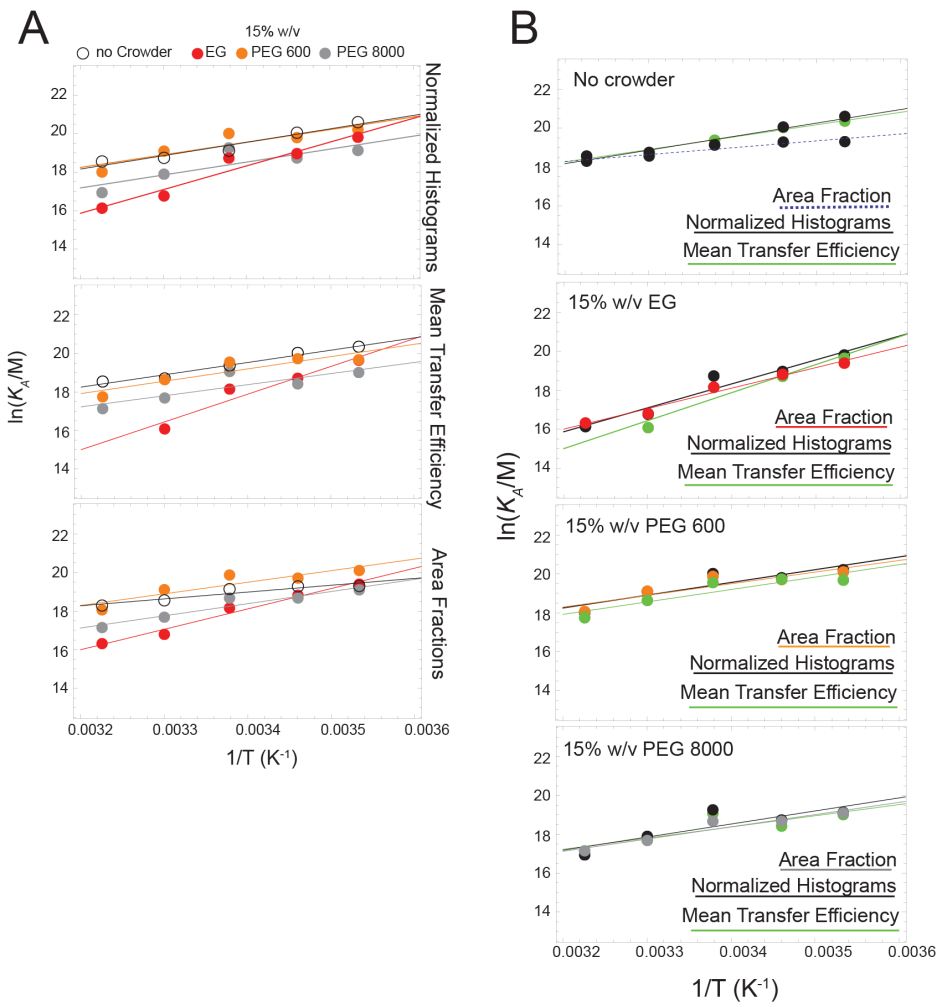


**Figure S11. Temperature dependence of ln($K_A$) as estimated from different fitting models.** Here we compared the temperature dependence of ln($K_A$) based on different methods of estimation: i) fitting the change in the area of normalized histograms based on the ; ii) fitting the change in the mean transfer efficiency; iii) analyzing the change in the area fractions obtained by fitting two Gaussian distributions on the transfer efficiency distribution. **A.** Comparison of ln($K_A$) across different PEG conditions (as indicated in the legend) for each of the methods. **B.** Comparison of ln($K_A$) for each individual set across the three different determination methods.

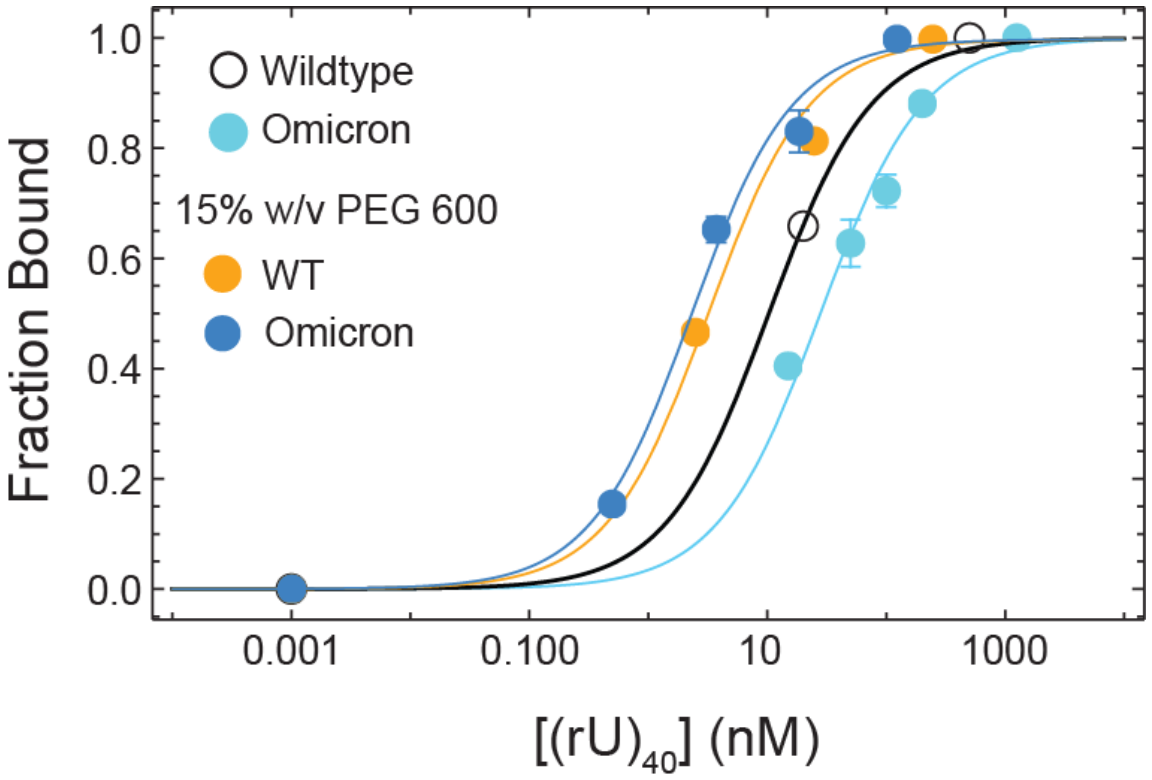


**Figure S12. Binding curves from single-molecule FRET experiments for wild type Wuhan-Hu-1 and Omicron variants in absence** (empty and cyan dots) **and presence** (orange and blue dots) **of 15% w/v PEG 600.**

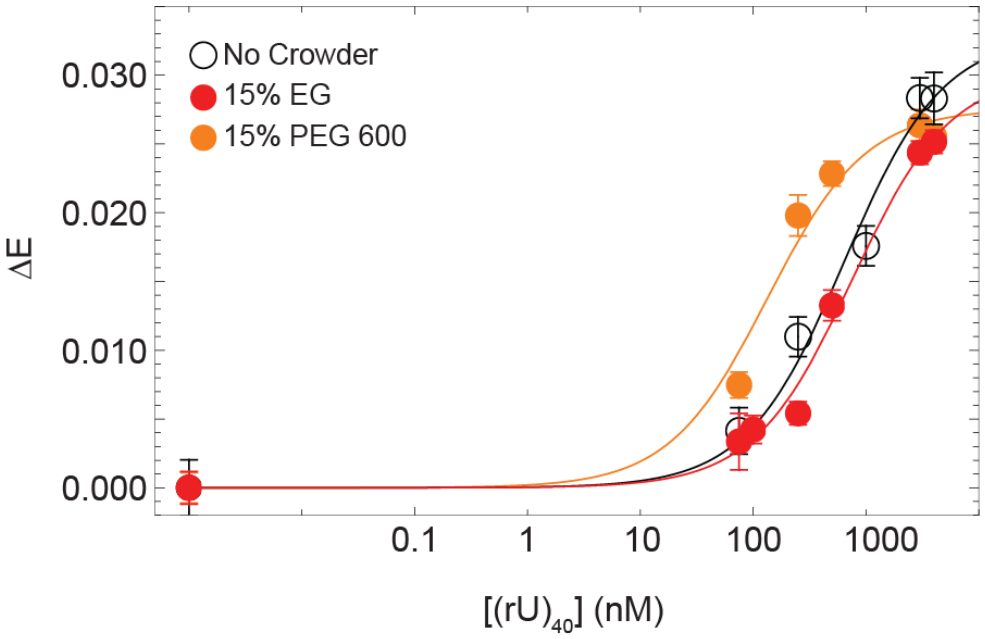


**Figure S13. Binding curves from single-molecule FRET experiments for $RBD_L$ in absence** (empty dots) **and presence of 15% w/v EG** (red dots) and **of 15% w/v PEG 600** (orange dots).

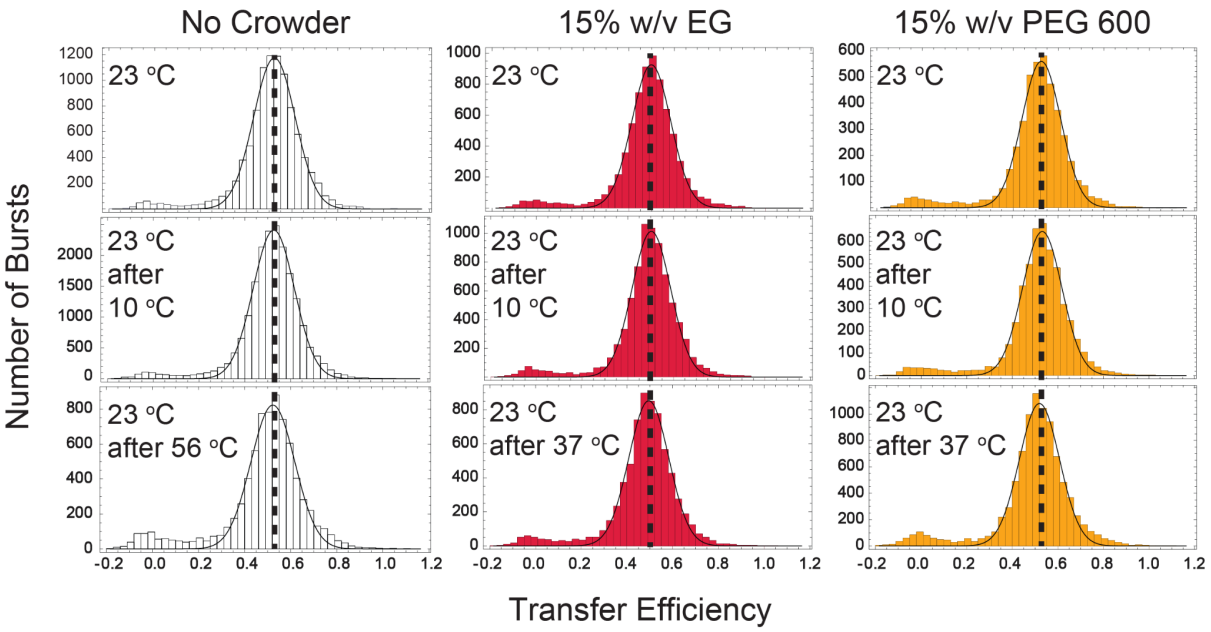


**Figure S14.** Transfer efficiency distributions of the $NTD_L$-RBD as a function of crowder concentrations (no crowder in white, EG in red, PEG 600 in orange) highlighting the reversible nature of the thermal response when bound to $(rU)_{40}$ (at a concentration of 500 nM).

## SUPPLEMENTARY TABLES.

**Table S1.** Sequence of WT NTD-RBD.

| | |
|---|---|
| **1** | **MSDNGPQNQR NAPRITFGGP SDSTGSNQNG ERSGARSKQR RPQGLPNNTA** |
| **51** | **SWFTALTQHG KEDLKFPRGQ GVPINTNSSP DDQIGYYRRA TRRIRGGDGK** |
| **101** | **MKDLSPRWYF YYLGTGPEAG LPYGANKDGI IWVATEGALN TPKDHIGTRN** |
| **151** | **PANNAAIVLQ LPQGTTLPKG FYA** |

**Table S2. Constructs used in this study.** For each construct, we reported the start and end positions compared to the wild type (WT) sequence, the labeling positions, and highlighted in purple the portion of the sequence in between the labeling positions.

| Name | Sequence | Start Position (WT) | End Position (WT) | Labeling Positions (WT) |
|---|---|---|---|---|
| **$NTD_L$-RBD** | GPCSDNGPQNQRNAPRITFGGPSDSTGSNQNGERSGARSKQRRPQGLPNNTASWFTALTQHGKEDLKFPCGQGVPINTNSSPDDQIGYYRRATRRIRGGDGKMKDLSPRWYFYYLGTGPEAGLPYGANKDGIIWVATEGALNTPKDHIGTRNPANNAAIVLQLPQGTTLPKGFYA | **1** | **173** | **1, 68** |
| **$NTD_L$-RBD Omicron (P13L, Δ31-33)** | GPCSDNGPQNQRNALRITFGGPSDSTGSNQNGGARSKQRRPQGLPNNTASWFTALTQHGKEDLKFPCGQGVPINTNSSPDDQIGYYRRATRRIRGGDGKMKDLSPRWYFYYLGTGPEAGLPYGANKDGIIWVATEGALNTPKDHIGTRNPANNAAIVLQLPQGTTLPKGFYA | **1** | **173** | **1, 68** |
| **$RBD_L$** | HHHHHHHHHLEVLFQGPSWFTALTQHGKEDLKFPCGQGVPINTNSSPDDQIGYYRRATRRIRGGDGKMKDLSPRWYFYYLGTGPEAGLPYGANKDGIIWVATEGALNTPKDHIGTRNPANNAAIVLQLPQGTTLPKGFYA | **51** | **173** | **68,172** |

**Table S3.** PEGs used in this study

| | **Company** | **Catalog Number** |
|---|---|---|
| **EG** | Sigma-Aldrich | 324558-100ML |
| **PEG 400** | Sigma-Aldrich | 202398-250G |
| **PEG 600** | Sigma-Aldrich | 87333-250G-F |
| **PEG 1000** | Sigma-Aldrich | 81189-100G |
| **PEG 2050** | Sigma-Aldrich | 295906-500G |
| **PEG 3350** | INTEGRA Chemical Company | P560.31.30 |
| **PEG 4600** | Sigma-Aldrich | 373001-250G |
| **PEG 6000** | EMD Millipore Corp. | 528877-100GM |
| **PEG 8000** | Sigma-Aldrich | 89510-250G-F |
| **PEG 35000** | Sigma-Aldrich | 94646-250G-F |

**Table S4.** Dynamics of the $NTD_L$-RBD in the presence of 15% Crowder.

| **NTD-RBD** | |
|---|---|
| | $\tau_{CD}\ (ns)$ |
| PEG 400 | 123 ± 4 |
| PEG 3350 | 119 ± 3 |

**Table S5. Schellman weak binding model individual fit results.** Values of *K* are not well defined because of the small amplitude or variation in data points, whereas value of *γ* can be determined more robustly from the amplitude change in Δε. Corresponding values of *γ* are reported in **Fig. 3D**.

| **individual fits** | ***K*** **($M^{-1}$)** | ***γ*** |
|---|---|---|
| **EG** | 1.2 ± 0.4 | 0.28 ± 0.05 |
| **PEG 400** | 1.9 ± 0.9 | 0.21 ± 0.05 |
| **PEG 600** | 0.4 ± 0.4 | 0.3 ± 0.3 |
| **PEG 1000** | 1.6 ± 0.8 | 0.13 ± 0.03 |
| **PEG 2050** | 50 ± 300 | 0.02 ± 0.02 |
| **PEG 3350** | 100 ± 300 | 0.02 ± 0.01 |
| **PEG 4600** | 100 ± 2000 | 0.008 ± 0.03 |
| **PEG 6000** | 0.6 ± 0.6 | 0.08 ± 0.05 |
| **PEG 8000** | 100 ± 800 | 0.01 ± 0.02 |
| **PEG 35000** | 100 ± 5000 | 0.005 ± 0.05 |

**Table S6. Schellman weak binding model global fit results.** Values of $K$, $\gamma_{ee}$, and $\gamma_{ii}$ are obtained based on **Eq. S12** and are reported in **Fig. 3A**. Note that Eq. S12 introduces a different definition of the concentrations and therefore the values in **Tables S4** and S**5** are not expected to be identical, though trends can be compared.

| **global fit** | $K$ **($M^{-1}$)** | $\gamma_{ee}$ | $\gamma_{ii}$ |
|---|---|---|---|
| | 1.3 ± 0.8 | 0.16 ± 0.03 | 0.037 ± 0.004 |

**Table S7.** Association constants for the binding of $NTD_L$-RBD to $(rU)_{40}$ in presence and absence of crowding agents at 23°C in 50 mM HEPES buffer.

| **15% w/v** | $K_A$ **for** $(rU)_{40}$ **($nM^{-1}$)** | $K_A/K_{A0}$ |
|---|---|---|
| **no crowders** | 0.097 ± 0.0061 | 1 |
| **EG** | 0.08 ± 0.02 | 0.82 ± 0.21 |
| **PEG 400** | 0.45 ± 0.07 | 4.6 ± 0.8 |
| **PEG 600** | 0.32 ± 0.04 | 3.3 ± 0.5 |
| **PEG 1000** | 0.21 ± 0.03 | 2.16 ± 0.34 |
| **PEG 2050** | 0.16 ± 0.02 | 1.65 ± 0.23 |
| **PEG 3350** | 0.43 ± 0.06 | 4.4 ± 0.7 |
| **PEG 8000** | 0.168 ± 0.001 | 1.73 ± 0.11 |
| **PEG 35000** | 0.098 ± 0.006 | 1.01 ± 0.09 |

**Table S8.** Association constants for the binding of $NTD_L$-RBD to $(rU)_{40}$ in presence and absence of 15% w/v crowding agents at temperatures from 10 °C to 37 °C in 50 mM HEPES buffer. Errors represent the error of the fit when analyzing the areas from the fraction bound.

| **$(rU)_{40}$** | **$K_A$ ($nM^{-1}$)** | | | | |
|---|---|---|---|---|---|
| **15% w/v** | **10 °C** | **16 °C** | **23 °C** | **30 °C** | **37 °C** |
| **no crowders** | 0.24 ± 0.01 | 0.24 ± 0.01 | 0.21 ± 0.07 | 0.11 ± 0.01 | 0.09 ± 0.01 |
| **EG** | 0.27 ± 0.01 | 0.15 ± 0.01 | 0.08 ± 0.01 | 0.02 ± 0.01 | 0.01 ± 0.01 |
| **PEG 600** | 0.54 ± 0.01 | 0.36 ± 0.01 | 0.43 ± 0.05 | 0.19 ± 0.01 | 0.07 ± 0.01 |
| **PEG 8000** | 0.20 ± 0.01 | 0.13 ± 0.01 | 0.12 ± 0.03 | 0.05 ± 0.01 | 0.028 ± 0.004 |

**Table S9.** Enthalpic and entropic contribution to the binding free energy in presence and absence of 15% w/v crowding agents at temperatures from 10 °C to 37 °C in 50 mM HEPES buffer. Errors associated with $\Delta\Delta H_{exp}$ and $\Delta\Delta S_{exp}$ are obtained through propagations of the errors.

| | | ΔH | ΔS | ΔΔH | ΔΔS | -TΔΔS at 23C |
|---|---|---|---|---|---|---|
| **noPEG** | | | | | | |
| | Mean E | -13 ± 1 | -0.004 ± 0.004 | | | |
| | Normalized Histo | -14 ± 2 | -0.008 ± 0.006 | | | |
| | Area Fracs | -7 ± 2 | 0.014 ± 0.005 | | | |
| **EG** | | | | | | |
| *No 37C | *Mean E | -29 ± 6 | -0.062 ± 0.019 | -16 ± 7 | -0.06 ± 0.02 | 17 ± 7 |
| | Normalized Histo | -24 ± 4 | -0.047 ± 0.012 | -10 ± 6 | -0.04 ± 0.02 | 11 ± 5 |
| | Area Fracs | -21 ± 2 | -0.035 ± 0.007 | -14 ± 3 | -0.049 ± 0.012 | 15 ± 4 |
| **PEG 600** | | | | | | |
| | Mean E | -13 ± 3 | -0.005 ± 0.011 | 0 ± 5 | -0.00 ± 0.02 | 0 ± 4 |
| | Normalized Histo | -13 ± 4 | -0.005 ± 0.013 | 1 ± 6 | 0.00 ± 0.02 | -1 ± 6 |
| | Area Fracs | -12 ± 3 | -0.002 ± 0.011 | -5 ± 5 | -0.016 ± 0.016 | 4 ± 5 |
| **PEG 8000** | | | | | | |
| | Mean E | -11 ± 4 | -0.002 ± 0.014 | 2 ± 5 | 0.00 ± 0.02 | -1 ± 5 |
| | Normalized Histo | -13 ± 5 | -0.009 ± 0.016 | 1 ± 7 | -0.00 ± 0.02 | 0.0 ± 7 |
| | Area Fracs | -12 ± 2 | -0.006 ± 0.008 | -6 ± 4 | -0.02 ± 0.013 | 6 ± 4 |

**Table S10**. Theoretical expectations from depletion theory ($\Delta\Delta S_{dt}$). $\Delta\Delta S_{dt}$ is computed assuming an effective radius of gyration for the RNA of 0.8 ± 0.3 nm. Errors associated with $\Delta\Delta S_{dt}$ are computed from the variation associated with the effective radius of gyration of RNA.

| **15% w/v** | **$\Delta\Delta S_{exp}$** (kcal/mol/K) | **$\Delta\Delta S_{dt}$** (kcal/mol/K) |
|---|---|---|
| **EG** | -0.02 ± 0.02 | 0.0014 (± 0.0003) |
| **PEG 600** | 0.01 ± 0.01 | 0.0021 (± 0.0006) |
| **PEG 8000** | 0.01 ± 0.01 | 0.0029 (+ 0.001, -0.0014) |

**Table S11.** Association constants for the binding of $RBD_L$ to $(rU)_{40}$ calculated using the change in mean transfer efficiencies in absence and presence of crowding agents in 50 mM HEPES buffer.

| | $K_A$ (nM$^{-1}$) | $K_A/K_{A0}$ |
|---|---|---|
| **50 mM HEPES** | 0.0016 ± 0.0004 | 1 |
| **15% EG** | 0.0012 ± 0.0003 | 0.8 ± 0.3 |
| **15% PEG 600** | 0.007 ± 0.002 | 4 ± 2 |

**REFERENCES.**


(1) van den Berg, J.; Boersma, A. J.; Poolman, B. Microorganisms Maintain Crowding Homeostasis. *Nat. Rev. Microbiol.* **2017**, *15* (5), 309–318.
(2) Zimmerman, S. B.; Trach, S. O. Estimation of Macromolecule Concentrations and Excluded Volume Effects for the Cytoplasm of Escherichia Coli. *J. Mol. Biol.* **1991**, *222* (3), 599–620.
(3) Cayley, S.; Record, M. T., Jr. Large Changes in Cytoplasmic Biopolymer Concentration with Osmolality Indicate That Macromolecular Crowding May Regulate Protein-DNA Interactions and Growth Rate in Osmotically Stressed Escherichia Coli K-12. *J. Mol. Recognit.* **2004**, *17* (5), 488–496.
(4) Boersma, A. J.; Zuhorn, I. S.; Poolman, B. A Sensor for Quantification of Macromolecular Crowding in Living Cells. *Nature Methods*. 2015, pp 227–229. https://doi.org/10.1038/nmeth.3257.
(5) Guin, D.; Gruebele, M. Weak Chemical Interactions That Drive Protein Evolution: Crowding, Sticking, and Quinary Structure in Folding and Function. *Chem. Rev.* **2019**, *119* (18), 10691–10717.
(6) Gnutt, D.; Timr, S.; Ahlers, J.; König, B.; Manderfeld, E.; Heyden, M.; Sterpone, F.; Ebbinghaus, S. Stability Effect of Quinary Interactions Reversed by Single Point Mutations. *J. Am. Chem. Soc.* **2019**, *141* (11), 4660–4669.
(7) Monteith, W. B.; Cohen, R. D.; Smith, A. E.; Guzman-Cisneros, E.; Pielak, G. J. Quinary Structure Modulates Protein Stability in Cells. *Proc. Natl. Acad. Sci. U. S. A.* **2015**, *112* (6), 1739–1742.
(8) Wirth, A. J.; Gruebele, M. Quinary Protein Structure and the Consequences of Crowding in Living Cells: Leaving the Test-Tube behind. *BioEssays*. 2013, pp 984–993. https://doi.org/10.1002/bies.201300080.
(9) Zhou, H.-X.; Rivas, G.; Minton, A. P. Macromolecular Crowding and Confinement: Biochemical, Biophysical, and Potential Physiological Consequences. *Annu. Rev. Biophys.* **2008**, *37*, 375–397.
(10) Ellis, R. J. Macromolecular Crowding: Obvious but Underappreciated. *Trends Biochem. Sci.* **2001**, *26* (10), 597–604.
(11) Minton, A. P. Implications of Macromolecular Crowding for Protein Assembly. *Curr. Opin. Struct. Biol.* **2000**, *10* (1), 34–39.
(12) Wang, Y.; Sarkar, M.; Smith, A. E.; Krois, A. S.; Pielak, G. J. Macromolecular Crowding and Protein Stability. *J. Am. Chem. Soc.* **2012**, *134* (40), 16614–16618.
(13) Elcock, A. H. Models of Macromolecular Crowding Effects and the Need for Quantitative Comparisons with Experiment. *Curr. Opin. Struct. Biol.* **2010**, *20* (2), 196–206.
(14) Soranno, A.; Koenig, I.; Borgia, M. B.; Hofmann, H.; Zosel, F.; Nettels, D.; Schuler, B. Single-Molecule Spectroscopy Reveals Polymer Effects of Disordered Proteins in Crowded Environments. *Proc. Natl. Acad. Sci. U. S. A.* **2014**, *111* (13), 4874–4879.
(15) Cubuk, J.; Soranno, A. Macromolecular Crowding and Intrinsically Disordered Proteins: A Polymer Physics Perspective. *ChemSystemsChem* **2022**. https://doi.org/10.1002/syst.202100051.
(16) André, A. A. M.; Spruijt, E. Liquid–Liquid Phase Separation in Crowded Environments. *Int. J. Mol. Sci.* **2020**, *21* (16), 5908.
(17) Kang, H.; Pincus, P. A.; Hyeon, C.; Thirumalai, D. Effects of Macromolecular

Crowding on the Collapse of Biopolymers. *Phys. Rev. Lett.* **2015**, *114* (6), 068303.
(18) Schuler, B.; König, I.; Soranno, A.; Nettels, D. Impact of In-cell and In-vitro Crowding on the Conformations and Dynamics of an Intrinsically Disordered Protein. *Angew. Chem. Weinheim Bergstr. Ger.* **2021**, No. ange.202016804. https://doi.org/10.1002/ange.202016804.
(19) König, I.; Zarrine-Afsar, A.; Aznauryan, M.; Soranno, A.; Wunderlich, B.; Dingfelder, F.; Stüber, J. C.; Plückthun, A.; Nettels, D.; Schuler, B. Single-Molecule Spectroscopy of Protein Conformational Dynamics in Live Eukaryotic Cells. *Nat. Methods* **2015**, *12* (8), 773–779.
(20) Qin, S.; Zhou, H.-X. Effects of Macromolecular Crowding on the Conformational Ensembles of Disordered Proteins. *J. Phys. Chem. Lett.* **2013**, *4* (20). https://doi.org/10.1021/jz401817x.
(21) Miller, C. M.; Kim, Y. C.; Mittal, J. Protein Composition Determines the Effect of Crowding on the Properties of Disordered Proteins. *Biophys. J.* **2016**, *111* (1), 28–37.
(22) Zosel, F.; Soranno, A.; Buholzer, K. J.; Nettels, D.; Schuler, B. Depletion Interactions Modulate the Binding between Disordered Proteins in Crowded Environments. *Proc. Natl. Acad. Sci. U. S. A.* **2020**, *117* (24), 13480–13489.
(23) Paudel, B. P.; Rueda, D. Molecular Crowding Accelerates Ribozyme Docking and Catalysis. *J. Am. Chem. Soc.* **2014**, *136* (48), 16700–16703.
(24) Daher, M.; Widom, J. R.; Tay, W.; Walter, N. G. Soft Interactions with Model Crowders and Non-Canonical Interactions with Cellular Proteins Stabilize RNA Folding. *J. Mol. Biol.* **2018**, *430* (4), 509–523.
(25) Schäfer, L.; Kappeler, C. A Renormalization Group Analysis of Ternary Polymer Solutions. *Journal de Physique* **1985**, *46* (11), 1853–1864.
(26) Schäfer, L.; Kappeler, C. Interaction Effects on the Size of a Polymer Chain in Ternary Solutions: A Renormalization Group Study. *J. Chem. Phys.* **1993**, *99* (8), 6135–6154.
(27) Schäfer, L. Excluded Volume Effects in Polymer Solutions. 1999. https://doi.org/10.1007/978-3-642-60093-7.
(28) Lekkerkerker, H. N. W.; Tuinier, R. Colloids and the Depletion Interaction. *Lecture Notes in Physics*. 2011. https://doi.org/10.1007/978-94-007-1223-2.
(29) Alston, J. J.; Ginell, G. M.; Soranno, A.; Holehouse, A. S. The Analytical Flory Random Coil Is a Simple-to-Use Reference Model for Unfolded and Disordered Proteins. *bioRxiv*, 2023, 2023.03.12.531990. https://doi.org/10.1101/2023.03.12.531990.
(30) Zheng, W.; Best, R. B. An Extended Guinier Analysis for Intrinsically Disordered Proteins. *J. Mol. Biol.* **2018**, *430* (16), 2540–2553.
(31) González-Foutel, N. S.; Glavina, J.; Borcherds, W. M.; Safranchik, M.; Barrera-Vilarmau, S.; Sagar, A.; Estaña, A.; Barozet, A.; Garrone, N. A.; Fernandez-Ballester, G. *et al*. Conformational Buffering Underlies Functional Selection in Intrinsically Disordered Protein Regions. *Nat. Struct. Mol. Biol.* **2022**, *29* (8), 781–790.
(32) Cubuk, J.; Alston, J. J.; Incicco, J. J.; Singh, S.; Stuchell-Brereton, M. D.; Ward, M. D.; Zimmerman, M. I.; Vithani, N.; Griffith, D.; Wagoner, J. A. *et al*. The SARS-CoV-2 Nucleocapsid Protein Is Dynamic, Disordered, and Phase Separates with RNA. *Nat. Commun.* **2021**, *12* (1), 1936.
(33) Cubuk, J.; Alston, J. J.; Jeremías Incicco, J.; Holehouse, A. S.; Hall, K. B.; Stuchell-Brereton, M. D.; Soranno, A. The Disordered N-Terminal Tail of SARS

CoV-2 Nucleocapsid Protein Forms a Dynamic Complex with RNA. *bioRxiv*, 2023, 2023.02.10.527914. https://doi.org/10.1101/2023.02.10.527914.
(34) Dupuis, N. F.; Holmstrom, E. D.; Nesbitt, D. J. Molecular-Crowding Effects on Single-Molecule RNA Folding/unfolding Thermodynamics and Kinetics. *Proc. Natl. Acad. Sci. U. S. A.* **2014**, *111* (23), 8464–8469.
(35) Sung, H.-L.; Sengupta, A.; Nesbitt, D. Smaller Molecules Crowd Better: Crowder Size Dependence Revealed by Single-Molecule FRET Studies and Depletion Force Modeling Analysis. *J. Chem. Phys.* **2021**, *154* (15), 155101.
(36) Stuchell-Brereton, M. D.; Zimmerman, M. I.; Miller, J. J.; Mallimadugula, U. L.; Incicco, J. J.; Roy, D.; Smith, L. G.; Cubuk, J.; Baban, B.; DeKoster, G. T.; Frieden, C.; Bowman, G. R.; Soranno, A. Apolipoprotein E4 Has Extensive Conformational Heterogeneity in Lipid-Free and Lipid-Bound Forms. *Proc. Natl. Acad. Sci. U. S. A.* **2023**, *120* (7), e2215371120.
(37) de Gennes, P.-G.; Gennes, P.-G. *Scaling Concepts in Polymer Physics*; Cornell University Press, 1979.
(38) Schuler, B.; Soranno, A.; Hofmann, H.; Nettels, D. Single-Molecule FRET Spectroscopy and the Polymer Physics of Unfolded and Intrinsically Disordered Proteins. *Annu. Rev. Biophys.* **2016**, *45*, 207–231.
(39) Sanchez, I. C. Phase Transition Behavior of the Isolated Polymer Chain. *Macromolecules* **1979**, *12* (5), 980–988.
(40) Sherman, E.; Haran, G. Coil-Globule Transition in the Denatured State of a Small Protein. *Proc. Natl. Acad. Sci. U. S. A.* **2006**, *103* (31), 11539–11543.
(41) Ziv, G.; Thirumalai, D.; Haran, G. Collapse Transition in Proteins. *Phys. Chem. Chem. Phys.* **2009**, *11* (1), 83–93.
(42) Hofmann, H.; Soranno, A.; Borgia, A.; Gast, K.; Nettels, D.; Schuler, B. Polymer Scaling Laws of Unfolded and Intrinsically Disordered Proteins Quantified with Single-Molecule Spectroscopy. *Proc. Natl. Acad. Sci. U. S. A.* **2012**, *109* (40), 16155–16160.
(43) Rubinstein, M.; Colby, R. H. *Polymer Physics*; Oxford University Press: New York, 2003.
(44) Schellman, J. A. Selective Binding and Solvent Denaturation. *Biopolymers* **1987**, *26* (4), 549–559.
(45) Schellman, J. A. Fifty Years of Solvent Denaturation. *Biophys. Chem.* **2002**, *96* (2-3), 91–101.
(46) Aznauryan, M.; Nettels, D.; Holla, A.; Hofmann, H.; Schuler, B. Single-Molecule Spectroscopy of Cold Denaturation and the Temperature-Induced Collapse of Unfolded Proteins. *J. Am. Chem. Soc.* **2013**, *135* (38), 14040–14043.
(47) Wuttke, R.; Hofmann, H.; Nettels, D.; Borgia, M. B.; Mittal, J.; Best, R. B.; Schuler, B. Temperature-Dependent Solvation Modulates the Dimensions of Disordered Proteins. *Proc. Natl. Acad. Sci. U. S. A.* **2014**, *111* (14), 5213–5218.
(48) Nettels, D.; Müller-Späth, S.; Küster, F.; Hofmann, H.; Haenni, D.; Rüegger, S.; Reymond, L.; Hoffmann, A.; Kubelka, J.; Heinz, B. *et al*. Single-Molecule Spectroscopy of the Temperature-Induced Collapse of Unfolded Proteins. *Proc. Natl. Acad. Sci. U. S. A.* **2009**, *106* (49), 20740–20745.
(49) Knowles, D. B.; Shkel, I. A.; Phan, N. M.; Sternke, M.; Lingeman, E.; Cheng, X.; Cheng, L.; O'Connor, K.; Record, M. T. Chemical Interactions of Polyethylene Glycols (PEGs) and Glycerol with Protein Functional Groups: Applications to Effects of PEG and Glycerol on Protein Processes. *Biochemistry* **2015**, *54* (22), 3528–3542.
(50) Shkel, I. A.; Knowles, D. B.; Record, M. T., Jr. Separating Chemical and

Excluded Volume Interactions of Polyethylene Glycols with Native Proteins: Comparison with PEG Effects on DNA Helix Formation. *Biopolymers* **2015**, *103* (9), 517–527.
(51) Stewart, C. J.; Olgenblum, G. I.; Propst, A.; Harries, D.; Pielak, G. J. Resolving the Enthalpy of Protein Stabilization by Macromolecular Crowding. *Protein Sci.* **2023**, *32* (3), e4573.
(52) Yoo, H.; Davis, C. M. An in Vitro Cytomimetic of in-Cell RNA Folding. *Chembiochem* **2022**, *23* (20), e202200406.
(53) Capp, M. W.; Pegram, L. M.; Saecker, R. M.; Kratz, M.; Riccardi, D.; Wendorff, T.; Cannon, J. G.; Record, M. T., Jr. Interactions of the Osmolyte Glycine Betaine with Molecular Surfaces in Water: Thermodynamics, Structural Interpretation, and Prediction of M-Values. *Biochemistry* **2009**, *48* (43), 10372–10379.
(54) Uversky, V. N. Intrinsically Disordered Proteins and Their Environment: Effects of Strong Denaturants, Temperature, pH, Counter Ions, Membranes, Binding Partners, Osmolytes, and Macromolecular Crowding. *Protein J.* **2009**, *28* (7-8), 305–325.
(55) Bar-On, Y. M.; Flamholz, A.; Phillips, R.; Milo, R. SARS-CoV-2 (COVID-19) by the Numbers. *Elife* **2020**, *9*. https://doi.org/10.7554/eLife.57309.
(56) Nettels, D.; Hoffmann, A.; Schuler, B. Unfolded Protein and Peptide Dynamics Investigated with Single-Molecule FRET and Correlation Spectroscopy from Picoseconds to Seconds. *J. Phys. Chem. B* **2008**, *112* (19), 6137–6146.
(57) Nettels, D.; Gopich, I. V.; Hoffmann, A.; Schuler, B. Ultrafast Dynamics of Protein Collapse from Single-Molecule Photon Statistics. *Proc. Natl. Acad. Sci. U. S. A.* **2007**, *104* (8), 2655–2660.
(58) Soranno, A. Physical Basis of the Disorder-Order Transition. *Arch. Biochem. Biophys.* **2020**, *685*, 108305.
(59) Müller-Späth, S.; Soranno, A.; Hirschfeld, V.; Hofmann, H.; Rüegger, S.; Reymond, L.; Nettels, D.; Schuler, B. From the Cover: Charge Interactions Can Dominate the Dimensions of Intrinsically Disordered Proteins. *Proc. Natl. Acad. Sci. U. S. A.* **2010**, *107* (33), 14609–14614.
(60) Instrumentation for Fluorescence Spectroscopy. In *Principles of Fluorescence Spectroscopy*; Lakowicz, J. R., Ed.; Springer US: Boston, MA, 2006; pp 27–61.
(61) Devanand, K.; Selser, J. C. Asymptotic Behavior and Long-Range Interactions in Aqueous Solutions of Poly(ethylene Oxide). *Macromolecules* **1991**, *24* (22), 5943–5947.
(62) Zhou, H. Effect of Interaction Potentials in Diffusion‐influenced Reactions with Small Reactive Regions. *The Journal of Chemical Physics*. 1996, pp 7235–7237. https://doi.org/10.1063/1.472530.
(63) Tuinier, R.; Lekkerkerker, H. N. W.; Aarts, D. G. A. L. Interaction Potential between Two Spheres Mediated by Excluded Volume Polymers. *Phys. Rev. E Stat. Nonlin. Soft Matter Phys.* **2002**, *65* (6 Pt 1), 060801.
(64) Hanke, A.; Eisenriegler, E.; Dietrich, S. Polymer Depletion Effects near Mesoscopic Particles. *Phys. Rev. E Stat. Phys. Plasmas Fluids Relat. Interdiscip. Topics* **1999**, *59* (6), 6853–6878.
(65) Fleer, G. J.; Tuinier, R. Analytical Phase Diagrams for Colloids and Non-Adsorbing Polymer. *Adv. Colloid Interface Sci.* **2008**, *143* (1-2), 1–47.